

Quantum simulation of the Hubbard model on a graphene hexagon: Strengths of IQPE and noise constraints

Mohammad Mirzakhani^{1,*} and Kyungsun Moon^{1,2,†}

¹*Department of Physics, Yonsei University, Seoul 03722, Korea*

²*Institute of Quantum Information Technology, Yonsei University, Seoul 03722, Korea*

Quantum computing offers transformative potential for simulating real-world materials, providing a powerful platform to investigate complex quantum systems across quantum chemistry and condensed matter physics. In this work, we leverage this capability to simulate the Hubbard model on a six-site graphene hexagon using Qiskit, employing the Iterative Quantum Phase Estimation (IQPE) and adiabatic evolution algorithms to determine its ground-state properties. Noiseless simulations yield accurate ground-state energies (GSEs), charge and spin densities, and correlation functions, all in excellent agreement with exact diagonalization, underscoring the precision and reliability of quantum simulation for strongly correlated electron systems. However, deploying IQPE and adiabatic evolution on today's noisy quantum hardware remains highly challenging. To examine these limitations, we utilize the Qiskit Aer simulator with a custom noise model tailored to the characteristics of IBM's real backend. This model includes realistic depolarizing gate errors, thermal relaxation, and readout noise, allowing us to explore how these factors degrade simulation accuracy. Preliminary hardware runs on IBM devices further expose discrepancies between simulated and real-world noise, emphasizing the gap between ideal and practical implementations. Overall, our results highlight the promise of quantum computing for simulating correlated quantum materials, while also revealing the significant challenges posed by hardware noise in achieving accurate and reliable physical predictions using current quantum devices.

I. INTRODUCTION

The intersection of quantum computing and materials science has emerged as a promising avenue for groundbreaking discoveries [1–3]. By leveraging the power of quantum algorithms, researchers aim to simulate complex quantum systems, such as those found in novel materials, with unprecedented accuracy and efficiency. One such system of significant interest is the Fermi-Hubbard model [4], a fundamental model in condensed matter physics that describes the behavior of interacting electrons on a lattice.

The Fermi-Hubbard model has long served as a fundamental framework for understanding the complex behavior of strongly correlated electron systems [5–9]. It captures key phenomena such as magnetism, superconductivity, and Mott insulator transitions [10], making it essential for exploring the physics of high-temperature superconductors, quantum spin liquids [11], and beyond. Despite its simplicity, solving the Hubbard model exactly for large systems remains a formidable challenge due to the exponential growth of the Hilbert space with system size. As of today, the largest Fermi-Hubbard system that has been solved exactly comprises 17 electrons on a 22-site lattice [12]. Conventional computational methods, such as density matrix renormalization group and quantum Monte Carlo, often face limitations, especially when addressing systems with strong correlations and intricate geometries [13, 14].

Quantum computing offers a new way to tackle the Fermi-Hubbard model, as it can potentially represent the full Hilbert space more efficiently, opening the door to studying larger, more realistic models that are classically intractable. The Fermi-Hubbard model has been extensively studied as a potential target for quantum simulation [15–26]. Its regular lattice structure and well-defined Hamiltonian, while presenting significant challenges for classical methods, make it an attractive benchmark for quantum algorithms.

Recent quantum simulations, particularly in quantum chemistry and materials science, have widely employed VQE (Variational Quantum Eigensolver) [27] and QAOA (Quantum Approximate Optimization Algorithm) [28] for quantum many-body systems like the Hubbard model [23, 25, 29, 30]. Such quantum-classical hybrid algorithms have been developed to overcome certain limitations. They involve training parameterized quantum circuits to minimize the energy of the system. For instance, VQE is an algorithm that leverages the power of quantum computers for optimization tasks and is particularly useful for finding ground-state energy (GSE). However, its practical application is limited by the high classical computational overhead, especially when advanced error mitigation is implemented.

On the other hand, recent advancements in quantum hardware open up significant opportunities. We may soon witness practical applications of quantum computing and the testing of fault-tolerant algorithms that were previously unattainable. While encouraging the development of fault-tolerant quantum algorithms, these advancements also encourage a critical evaluation of near-term quantum approaches, exploring their potential utility across various scenarios. Among these, Quantum

* mohamad.mirzakhani@gmail.com

† kmoon@yonsei.ac.kr

Phase Estimation (QPE) [31] stands out as a cornerstone algorithm for realizing many quantum computing applications. QPE is crucial for tasks such as calculating molecular energies in quantum chemistry, solving eigenvalue problems, and advancing materials science—all of which benefit from the precision and scalability offered by fault-tolerant quantum computing.

While less directly applied to the Hubbard model, QPE is also particularly well-suited for determining the ground-state properties of quantum systems [16, 32–36]. Combining the strengths of phase estimation and iterative algorithms, iterative QPE (IQPE) provides a resource-efficient method for approximating GSEs [36–39]. Abrams and Lloyd [33] were the pioneers in exploring time evolution governed by the Hubbard Hamiltonian, albeit without presenting concrete quantum circuit implementations. In Ref. [34] they provide further details that the use of QPE can project trial states onto the corresponding energy eigenstates. Technical details on simulating the Fermi-Hubbard model using phase estimation algorithm can be found in Refs. [16, 36].

In this work, we focus on simulating the Hubbard model on a six-site graphene hexagon, a minimal yet representative unit that encapsulates the material’s correlated electron behavior. Leveraging Qiskit [40], an open-source quantum computing framework, we employ the IQPE algorithm to probe the system’s ground-state properties with high precision in a noiseless environment. This approach, complemented by adiabatic time evolution, allows us to compute GSEs, charge and spin densities, and charge and spin correlations, providing a detailed understanding of graphene’s electronic structure. To validate the power of this quantum method, we benchmark our results against exact diagonalization, achieving excellent agreement and underscoring its capability to accurately model real materials.

Yet, the transition from idealized simulations to practical quantum hardware introduces significant hurdles. IQPE, while powerful, demands deep circuits and precise control, making it particularly sensitive to noise in noisy intermediate-scale quantum (NISQ) devices. To investigate these challenges, we utilize the Qiskit Aer simulator [41] with a noise model tailored to IBM’s superconducting qubit platform [42], incorporating gate-specific depolarizing errors, thermal relaxation, and readout noise. This noisy simulation reveals both the robustness of our results and their degradation under realistic conditions. Further, we present preliminary experiments on IBM quantum hardware, providing a direct comparison with simulated noise and highlighting discrepancies between simulated and physical noise behavior, underscoring the need for improved calibration and algorithmic resilience. This work demonstrates both the promise and the current limitations of quantum computing for materials simulation. It offers a step toward benchmarking quantum algorithms for strongly correlated systems and serves as a case study for evaluating the performance of IQPE under realistic noise conditions.

II. THEORY AND MODEL

A. Graphene fragments and the Hubbard Model

The Hubbard model, a fundamental framework in condensed matter physics, captures the essential physics of electrons in a lattice by incorporating electron-electron (e-e) interactions and hopping between neighboring sites [5, 8, 9]. It is particularly effective in describing strongly correlated phenomena such as magnetism, metal-insulator transitions, and superconductivity. In the context of graphene—a material with a hexagonal lattice where each carbon atom contributes a p_z orbital to the delocalized π -band—the Hubbard model provides a natural description of its low-energy electronic and magnetic properties [43, 44]. For finite graphene structures, often referred to as nanoflakes or quantum dots, adaptations of the tight-binding and Hubbard models are used to capture size and edge effects, which play a crucial role in determining the system’s electronic behavior [45–49]. Here, we consider the smallest possible graphene fragment: a single hexagonal unit of the graphene honeycomb lattice, consisting of six carbon atoms positioned at its vertices, as illustrated in Fig. 1(a).

The Hamiltonian of the Hubbard model consists of two main terms that describe the competing effects of electron hopping (H_0) and on-site e-e repulsion (H_U) [4]:

$$\mathcal{H} = H_0 + H_U. \quad (1)$$

The first term, H_0 , is the single-particle tight-binding Hamiltonian, representing the movement of electrons between adjacent lattice sites. In the second quantization formalism, it can be written as

$$\mathcal{H}_0 = \sum_{i,\sigma} \epsilon_{i\sigma} a_{i\sigma}^\dagger a_{i\sigma} - \gamma_0 \sum_{\langle i,j \rangle, \sigma} \left(a_{i\sigma}^\dagger a_{j\sigma} + \text{h.c.} \right). \quad (2)$$

Here, $a_{i\sigma}^\dagger$ and $a_{j\sigma}$ are the electron creation and annihilation operators, respectively, which add or remove an electron with spin σ at sites i and j . $\epsilon_{i\sigma}$ and γ_0 are the on-site and hopping energies, respectively. Here, we set $\epsilon_{i\sigma} = 0$ and $\gamma_0 = 1$. The sum $\langle i, j \rangle$ restricts this interaction to nearest-neighbor sites.

The second term in Hamiltonian (1) is the Hubbard term that introduces e-e interactions through the repulsive on-site Coulomb interaction,

$$\mathcal{H}_U = U_0 \sum_i n_{i\uparrow} n_{i\downarrow}, \quad (3)$$

where $n_{i\sigma} = a_{i\sigma}^\dagger a_{i\sigma}$ ($\sigma = \uparrow, \downarrow$) is the spin-resolved electron density at site i . The parameter $U_0 > 0$ is the Hubbard parameter and denotes, in the short-range regime, the on-site Coulomb repulsion energy for each pair of electrons with opposite spins on the same site i .

B. Quantum computing approach

QPE is a quantum algorithm that enables us to efficiently estimate the eigenvalues of a given Hamiltonian [16, 35, 36]. This capability is essential for finding the ground state and low-energy excited states of a system, which are critical for determining its electronic and magnetic properties. IQPE is a simplified and resource-efficient variant of QPE [36–38]. Unlike standard QPE, IQPE estimates the phase iteratively, qubit by qubit, and does not require an ancillary qubit register for each bit of precision. This makes it more practical for near-term quantum devices with limited qubit resources. In theory, the algorithm’s accuracy is constrained only by the number of iterations. However, in practice, it is limited by experimental imperfections. The highest experimentally achievable accuracy can act as a benchmark for evaluating the performance and identifying limitations of IQPE algorithm implementations on current NISQ devices. We take the following approach to simulate the Hubbard model on a quantum hardware.

1. Preparing initial state

The success of the IQPE algorithm largely depends on the choice of the initial state, as it must have a significant overlap with the target eigenstate of the Hamiltonian being solved, here, the ground state of the Hubbard model. However, achieving a perfect overlap with the ground state is not essential; if the overlap is sufficiently large, we can apply phase estimation algorithm to the state and still have a reasonably large chance of projecting onto the ground state.

Slater determinant (SD): For fermionic systems like the Hubbard model, a natural choice for an initial state is an SD. An SD can be regarded as an eigenstate of a quadratic Hamiltonian, or simply as a wavefunction that describes a set of non-interacting fermions that can be represented as a product of single-particle states. The standard method for preparing SDs was introduced in Ref. [50] and later optimized in Refs. [16, 51] using Givens rotations—elementary operations that perform rotations in the plane defined by two coordinate axes. Jiang *et al.* in Ref. [18] improved the existing algorithm to prepare an arbitrary SD by exploiting a unitary symmetry.

Annealed initial state: Although it is simple to prepare on a quantum computer, an SD might not always have a high overlap with the true correlated ground state of a strongly interacting system. If the overlap with the target ground state is low, an *annealed* state can be used as an approximation of the ground state of the full Hubbard Hamiltonian. This state generally has a much higher overlap with the actual ground state than a simple SD. To prepare an annealed state as an initial state, one can use an adiabatic state preparation technique [35, 52]. This process involves gradually evolving from the ground state of a known Hamiltonian, such as a

SD from Hartree-Fock, to the ground state of the target Hubbard Hamiltonian. To achieve this, we introduce a smoothly varying adiabatic path Hamiltonian:

$$\mathcal{H}_{\text{ad}}(\eta) = (1 - \eta(t))\mathcal{H}_0 + \eta(t)\mathcal{H}, \quad (4)$$

where $0 \leq \eta(t) \leq 1$. A common choice is $\eta(t) = t/T$, where T is the total evolution time, though alternative schedules (e.g., nonlinear variations) can optimize the process. Adiabatic state preparation is efficient when T satisfies the following condition:

$$T \gg \Delta_{\text{min}}(\eta)^{-2}, \quad (5)$$

where $\Delta_{\text{min}}(\eta)$ is the minimum energy gap between the ground state and the first excited state of $\mathcal{H}_{\text{ad}}(\eta)$ during evolution. For a more comprehensive discussion on state preparation techniques, including the adiabatic approach, see Refs. [16, 36] and references therein.

Here, however, due to the small size of our system, we utilize SDs as the initial state, prepared using the algorithm in Ref. [18] and implemented in Qiskit Nature [53]. Our numerical results demonstrate the effectiveness of these initial states in achieving reasonably accurate results with the IQPE algorithm.

2. Unitary time evolution of the Hubbard model

The core of IQPE algorithm involves simulating the time evolution of the system under the Hubbard Hamiltonian (1), represented by the unitary operator $\mathcal{U}_{\mathcal{H}}(t) = \exp(-i\mathcal{H}t)$. This unitary evolution can be approximated using techniques like Trotterization [54], which breaks down the exponential of the Hamiltonian into a sequence of gates. This section outlines the Trotter decomposition for non-commuting Hamiltonian terms and provide explicit quantum circuit constructions for the relevant exponentials.

Trotter-Suzuki decomposition: Trotterization, often referred to as Trotter-Suzuki decomposition, is a key technique in quantum computing used to approximate the time evolution of quantum systems by decomposing the total evolution into a product of evolutions for individual Hamiltonian terms. Suppose the Hamiltonian \mathcal{H} can be decomposed as a sum of terms $\mathcal{H} = \mathcal{H}_1 + \mathcal{H}_2 + \dots + \mathcal{H}_k$, where each term \mathcal{H}_i represents a distinct part of the system, such as interactions or kinetic energy components. Because these terms do not generally commute, the first-order Trotter-Suzuki decomposition approximates the evolution operator as:

$$e^{-i\mathcal{H}t} \approx (e^{-i\mathcal{H}_1\Delta t} e^{-i\mathcal{H}_2\Delta t} \dots e^{-i\mathcal{H}_k\Delta t})^{N_{\text{trot}}}, \quad (6)$$

where $\Delta t = t/N_{\text{trot}}$ and N_{trot} is the number of Trotter steps [54]. As N_{trot} increases, the approximation becomes more accurate. By applying the Trotterized sequence of these smaller exponentiated terms, we can approximate the evolution of our system on a quantum computer.

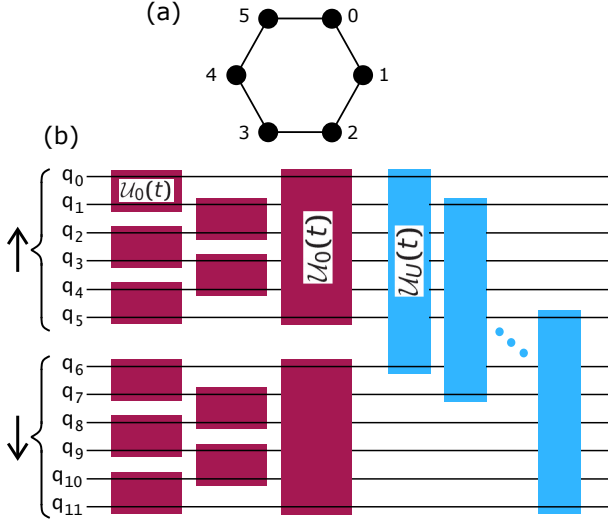


FIG. 1. (a) Graphene hexagon with six atomic sites labeled from 0 to 5. (b) A schematic quantum circuit for the time evolution under the Hubbard model Hamiltonian (1). The first $N = 6$ qubits correspond to spin-up states, while the remaining $N = 6$ qubits represent spin-down states. The red boxes, $\mathcal{U}_0(t)$, implement the time evolution under the hopping terms between two adjacent atomic sites. The blue boxes, $\mathcal{U}_U(t)$, represent the time evolution under the on-site Coulomb interaction between qubits of opposite spins, i.e., q_i and q_{N+i} . Details of the unitary operators $\mathcal{U}_0(t)$ and $\mathcal{U}_U(t)$ are provided in the Appendix.

Quantum circuits: In order to simulate a fermionic Hamiltonian on a quantum computer, one needs to use the well-known Jordan-Wigner (JW) transformation, which maps each fermionic mode to a single qubit arranged along a 1D line [50, 55]. In the JW transformation, each fermionic mode (which can be either occupied or unoccupied) is mapped to a spin-1/2 system (a qubit), where the presence or absence of a fermion corresponds to the qubit being in the $|1\rangle$ or $|0\rangle$ state. The transformation uses Pauli operators (X, Y, Z, I) to capture the creation and annihilation of fermions, with careful handling of the anti-commutation relationships. Specifically, a string of Pauli Z operators is introduced to maintain the correct anti-commutation properties, which is essential for ensuring that fermionic operators act properly in the quantum simulation.

In the case of Hubbard model, we need to implement unitary evolution under two types of terms: hopping terms $h_0 = -\gamma_0(a_{i\sigma}^\dagger a_{j\sigma} + a_{j\sigma}^\dagger a_{i\sigma})$ and on-site Coulomb interactions $h_U = U_0 n_{i\sigma} n_{i\sigma'}$. To establish the necessary notation, we present the explicit Pauli representation of the Hubbard model and outline the corresponding quantum circuits (see Appendix) used to solve the Hubbard model in this paper.

Using the JW transformation for the hopping terms h_0 in (2), we can derive the following expression for the case

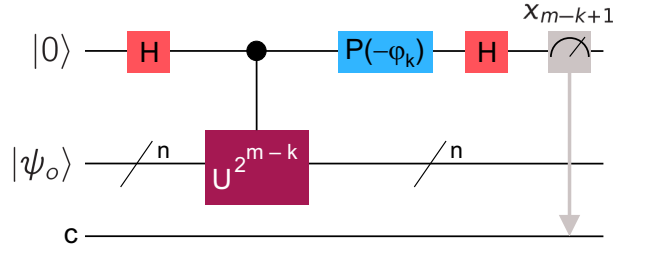


FIG. 2. The IQPE algorithm for the k th iteration. In the circuit, $|\psi_o\rangle$ is an eigenstate of U , and the angle φ_k of the phase gate depends on the previously measured bits defined as $\varphi_k = 0.x_{m-k+2}x_{m-k+1}x_m$ binary, where m is the number of digits determining the accuracy of the phase ϕ_o . Note that φ_k is zero in the first iteration of the algorithm.

$j > i$:

$$(a_i^\dagger a_j + a_j^\dagger a_i) \mapsto \frac{1}{2}(X_i X_j + Y_i Y_j) Z_{JW}, \quad (7)$$

where $Z_{JW} = Z_{i+1} \dots Z_{j-1}$. In the Hamiltonian \mathcal{H}_0 (2), certain terms may act on more than two qubits through a Z_{JW} string depending on the arrangement of the lattice sites. The corresponding quantum circuit for the time evolution under the hopping terms h_0 , i.e., $\mathcal{U}_0(t) = \exp(-ih_0 t)$, is provided in the Appendix. Using a similar approach, we can express the number and Coulomb-interaction operators in terms of Pauli matrices, respectively:

$$n_i = a_i^\dagger a_i = \frac{1}{2}(I_i - Z_i), \quad (8)$$

$$n_i n_j = \frac{1}{4}(I_i I_j - I_i Z_j - Z_i I_j + Z_i Z_j). \quad (9)$$

For the circuits that implement the time evolution of these operators, refer to the Appendix.

For graphene fragments with N atoms, the numbering of atomic sites shown in Fig. 1(a) enables us to map the lattice onto a qubit line. We arrange the $2N$ qubits such that the first N qubits, indexed by the lattice-site positions, correspond to spin-up states and the remaining N qubits correspond to spin-down states, so that $a_{i\uparrow}^\dagger = a_i^\dagger$ and $a_{i\downarrow}^\dagger = a_{i+N}^\dagger$. This ordering simplifies the JW strings required, as the hopping terms conserve spin.

With this pattern, we demonstrate in Fig. 1(b) the corresponding circuit for a graphene hexagon with $N = 6$ that implements time evolution for a time step t under the Hubbard Hamiltonian in Eq. 1. In this circuit, $\mathcal{U}_0(t)$ (red boxes) implements the time evolution of the hopping terms between neighboring sites according to their ordered indices within each spin state. The operation $\mathcal{U}_U(t) (\equiv \exp(-ih_U t))$, blue boxes) corresponds to the on-site Coulomb interaction between spin-up and spin-down states, acting between pairs of qubits with opposite spins, specifically q_i and q_{i+N} where $i = 0, 1, \dots, 5$.

3. IQPE

Here, we briefly describe the IQPE algorithm, which has been extensively detailed in many studies (see, e.g., Refs. [36–38]). IQPE is an adaptation of the QPE algorithm, widely used in quantum computing for tasks such as solving eigenvalue problems and simulating quantum systems [15, 16, 36].

As shown in Fig. 2, the IQPE algorithm for solving an eigenvalue problem requires two inputs: (1) an initial state $|\psi_o\rangle$ that is close to an eigenstate of the system's Hamiltonian \mathcal{H} , and (2) a unitary operator $\mathcal{U} [\equiv \exp(-i\mathcal{H}t)$ with eigenvalue $\exp(i2\pi\phi_o)$], which represents the time evolution of the system. The process begins by preparing the system in the eigenstate $|\psi_o\rangle$ and initializing an ancillary qubit in the state $|+\rangle = (|0\rangle + |1\rangle)/\sqrt{2}$ (the first Hadamard (H) gate in Fig. 2). A controlled- $\mathcal{U}^{2^{m-k}}$ operation is then applied, where $k = 1, 2, \dots, m$ denotes the iteration index and m represents the desired number of binary digits determining the precision of a phase parameter $\phi_o = 0.x_1x_2\dots x_m$. In the first iteration ($k = 1$), a controlled- $\mathcal{U}^{2^{m-1}}$ operation and $P(\varphi_1 = 0)$ are applied. The control qubit is then measured in the computational basis following the application of the second H gate, yielding the first bit x_m of the phase expansion. Next, we update the phase estimate $\varphi_2 = 0.0x_m$ for $P(\varphi_2)$, preparing for the second iteration ($k = 2$). In the k th iteration, a controlled- $\mathcal{U}^{2^{m-k}}$ operation and $P(\varphi_k)$ are applied, where $\varphi_k = 0.0x_{m-k+2}x_{m-1}x_m$, updated from previous iterations. This measurement result is used to refine the phase estimate, determining x_{m-k+1} . The algorithm concludes when the final bit x_1 is obtained in the $k = m$ iteration. By iteratively repeating these steps and incrementing k during each iteration, the algorithm successively refines the phase estimate, determining each bit with increasing accuracy. Once the phase is estimated, the corresponding eigenvalue of the Hamiltonian can be computed as $E_o = -2\pi\phi_o/t$.

III. NUMERICAL RESULTS

A. Noiseless simulation

We begin by computing the GSE for all occupation numbers $1 \leq N_{\text{occ}} \leq 11$, considering both the non-interacting case ($U_0 = 0$) and the presence of on-site interaction energy ($U_0 = 3$), as shown in Figs. 3(a) and 3(b), respectively. We simulate our structure using the noiseless Qiskit Aer simulator and use exact diagonalization results obtained with the QuSpin package [56] as a benchmark for comparison. In the case of the IQPE algorithm, we obtain results with a binary precision of $m = 5$ digits. To accurately recover E_o , t must be chosen such that the phase $E_o t$ remains in the range $[0, 2\pi)$ (or equivalently $\phi_o \in [0, 1)$) to avoid phase wrapping and ambiguity. The exact value of t depends on the energy

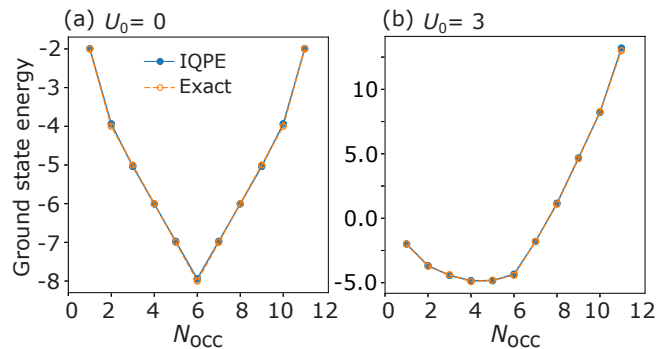


FIG. 3. GSE as a function of occupation number N_{occ} for a Hubbard model on a graphene hexagon lattice. (a) Non-interacting case ($U_0 = 0$) and (b) interacting case ($U_0 = 3$). Filled blue circles represent (noiseless) IQPE results, while open orange circles denote exact diagonalization. The close agreement between IQPE and exact results demonstrates the accuracy of the quantum algorithm.

scale of the system; often it is chosen such that even the maximum eigenvalue of interest satisfies $E_{\text{max}}t < 2\pi$. However, if t is too large, the phase might wrap around (i.e., become modulo 2π), leading to ambiguities. Therefore, t must be chosen based on an estimate of the energy spectrum of \mathcal{H} . In practice, one might choose t based on prior knowledge of the system's energy scale or by performing preliminary runs to determine a suitable scaling. For the time evolution under $\mathcal{U}_{\mathcal{H}}(t)$, we employ a Trotterization scheme with $N_{\text{trot}} = 15$ steps as explained in Sec. II B.

Figure 3 demonstrate the GSE as a function of occupation number N_{occ} for a graphene hexagonal lattice described with the Hubbard model. We observe a strong quantitative agreement between the exact diagonalization (orange open circles) and IQPE results (blue filled circles), demonstrating the accuracy and reliability of the IQPE method in capturing GSEs. In the non-interacting case ($U_0 = 0$), Fig. 3(a) shows a symmetric V-shaped dependence, reflecting the expected energy behavior dominated by kinetic terms. In this case, as seen, the half-filling configuration has the lowest GSE. In the interacting case [$U_0 = 3$, Fig. 3(b)], GSE shows a significant deviation from the non-interacting trend, with a flatter minimum and an upward energy shift due to the on-site Coulomb repulsion. The lowest GSE varies with the interaction strength U_0 , occurring at different occupation numbers depending on its magnitude. For instance, at $U_0 = 3$, the lowest GSE is found for $N_{\text{occ}} = 4$ as seen in Fig. 3(b). Despite the presence of interactions, IQPE still remains highly accurate, while using the SD as the initial state. These findings highlight the capability of IQPE in accurately determining eigenvalues, demonstrating its potential for simulating strongly correlated systems using quantum computing.

Below, we analyze the impact of bit precision m and Trotter step number N_{trot} on the accuracy of IQPE results. In Figs. 4(a) and 4(b), we depict the convergence

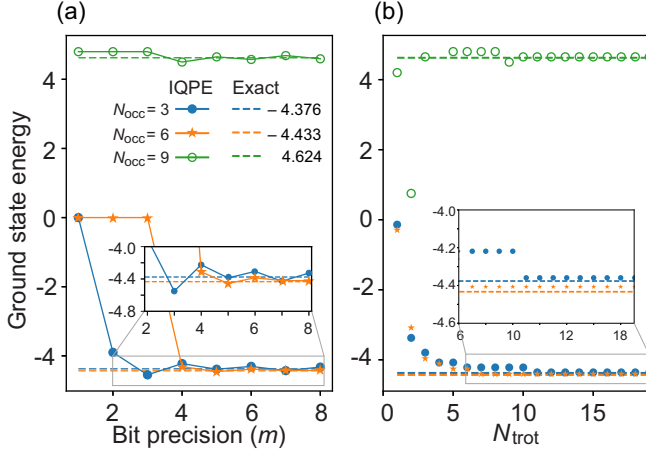


FIG. 4. Convergence of the GSE as a function of (a) bit precision m with $N_{\text{trot}} = 15$ and (b) Trotter step number N_{trot} with $m = 5$ for three different occupation numbers $N_{\text{occ}} = 3, 6$ and 9 . Results are shown for the interacting case with $U_0 = 3$.

of the GSE as a function of binary precision m (with $N_{\text{trot}} = 15$) and Trotterization steps N_{trot} (with $m = 5$) for three different occupation numbers $N_{\text{occ}} = 3, 6$, and 9 , respectively. The on-site potential is $U_0 = 3$. As seen, only within a few iterations, IQPE algorithm is enable to converge to the exact value with the high accuracy. For the structure studied here, selecting optimal values of $N_{\text{trot}} = 15$ and $m = 5$ yields highly accurate (noiseless) results, which are also feasible for execution on current quantum hardware.

Next, we study the dependence of the GSE on the on-site potential, U_0 , for a range of occupation numbers, $3 \leq N_{\text{occ}} \leq 9$, as presented in Fig. 5. Symbols represent the IQPE results, while dashed lines indicate the exact diagonalization outcomes. The excellent agreement between IQPE and exact results demonstrates the accuracy and reliability of the IQPE algorithm in capturing the GSE of the Hubbard model across various interaction strengths and particle fillings. As expected, the GSE generally increases with increasing on-site interaction strength. This behavior arises from the repulsive nature of the on-site interaction term, which penalizes configurations with double occupancy of lattice sites. The energies for different N_{occ} exhibit distinct behavior. For larger N_{occ} , the energy increases more rapidly with U_0 compared to smaller N_{occ} . This is expected since more electrons lead to stronger interaction effects. As seen, for small U_0 , energy differences are larger, but as U_0 increases, the trends become more parallel, suggesting that strong interactions dominate over kinetic contributions. For $U_0/\gamma_0 \lesssim 2$, the half-filled configuration exhibits the lowest GSE. However, beyond $U_0 \approx 2$, the configurations with $N_{\text{occ}} = 5$ (for a short range) and $N_{\text{occ}} = 4$ become the lowest-energy states as U_0 increases.

Following, we analyze the behavior of charge and spin densities (n_i, s_i) along with the charge and spin correla-

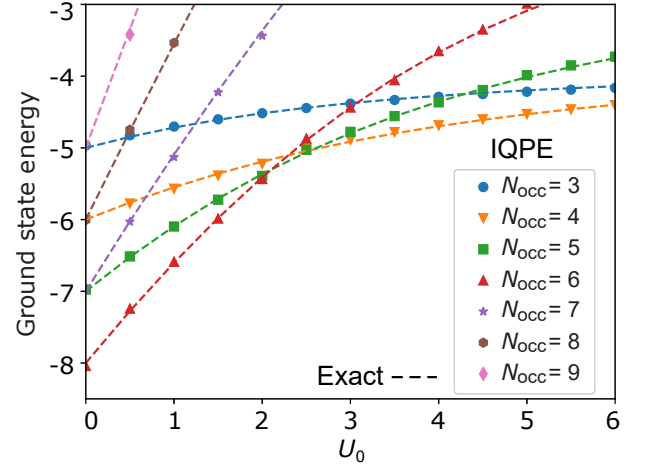


FIG. 5. The GSE as a function of the on-site interaction strength U_0 for occupation numbers $3 \leq N_{\text{occ}} \leq 9$. Symbols represent IQPE results, while the dashed curves correspond to exact diagonalization results. The IQPE results are obtained using a binary precision of $m = 5$ and Trotter step number of $N_{\text{trot}} = 15$.

tions ($C_{i,j}^c, C_{i,j}^s$), which are respectively defined as:

$$n_i = n_{i\uparrow} + n_{i\downarrow}, \quad (10)$$

$$S_i^z = n_{i\uparrow} - n_{i\downarrow}, \quad (11)$$

$$C_{i,j}^c = \langle n_i n_j \rangle - \langle n_i \rangle \langle n_j \rangle, \quad (12)$$

$$C_{i,j}^s = \langle S_i^z S_j^z \rangle - \langle S_i^z \rangle \langle S_j^z \rangle. \quad (13)$$

For this purpose, we utilize the adiabatic evolution method introduced in Sec. II B 1. In this study, we consider a linear evolution path, given by $\eta(t) = t/T$.

Figure 6 shows the distribution of (a) charge densities and (b) spin densities across the six atomic sites for different occupation numbers ($2 \leq N_{\text{occ}} \leq 10$) at $U_0 = 3$. The dashed lines represent the exact diagonalization densities while the empty circles correspond to the adiabatic-evolution results. As seen, the quantum simulation results closely follow the exact diagonalization results for all N_{occ} . This suggests that the quantum annealing algorithm is performing well in capturing the ground state of the system, at least for this small system size. Charge densities for all odd occupation numbers exhibit similar trends [Fig. 6(a)]. For each odd N_{occ} , the charge densities fluctuates across sites, averaging around $N_{\text{occ}}/6$. Site-dependent fluctuations in charge density arise due to electron interactions and quantum effects. However, these fluctuations exhibit a repeating pattern beyond three atomic sites, reflecting the underlying symmetry of the system. Additionally, the difference between the charge densities for successive odd occupation numbers remains nearly constant. This difference is approximately ≈ 0.33 , which corresponds to the average charge density of an electron pair ($\uparrow\downarrow$) uniformly distributed across the six atomic sites. This suggests a systematic charge accumulation as the electron number increases, maintaining a balanced distribution within the lattice.

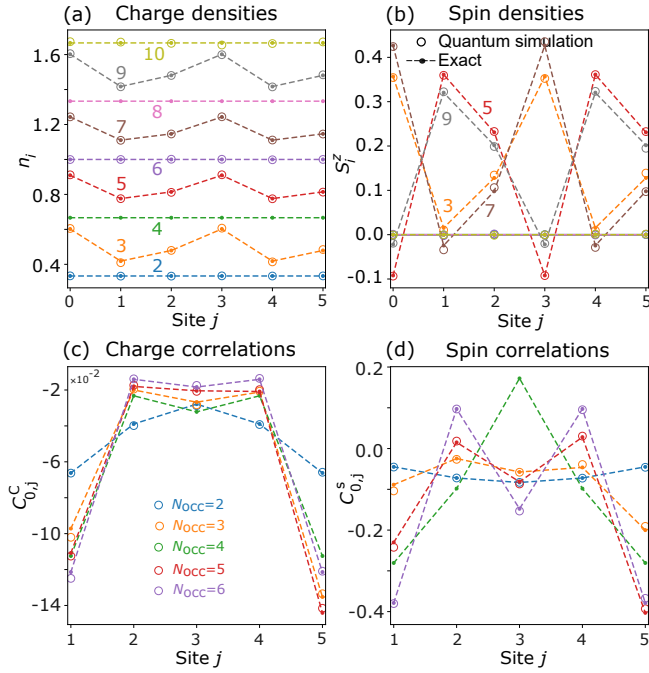


FIG. 6. Comparison of (a) charge densities n_i , (b) spin densities S_i^z , (c) charge correlations $C_{0,j}^c$, and (d) spin correlations $C_{0,j}^s$ obtained from adiabatic quantum simulation (empty circles) and exact diagonalization (dashed lines). The interaction strength is $U_0 = 3$. Results are presented for different occupation numbers, as indicated in each panel. The excellent agreement between methods demonstrates the accuracy of quantum simulation in capturing electronic correlations.

The corresponding spin densities for odd N_{occ} [Fig. 6(b)] alternate significantly between lattice sites, forming a staggered pattern. The alternating positive and negative spin densities suggest an antiferromagnetic-like arrangement, where neighboring sites preferentially adopt opposite spin orientations. In contrast to the smoothly varying charge densities, spin densities exhibit sharper oscillations with clear site-to-site alternation. This behavior is characteristic of correlated systems, where electrons tend to avoid double occupancy to minimize interaction energy, leading to pronounced spin polarization. Notably, the spin densities for odd occupation numbers exhibit mirrored patterns. This symmetry arises because of particle-hole conjugation and the intrinsic properties of the Hubbard Hamiltonian on a bipartite lattice.

For fully paired electron configurations, i.e., even N_{occ} , the charge densities are uniformly distributed across the atomic sites, Fig. 6(a). This suggests that, in the absence of unpaired electrons, the charge distribution becomes more homogeneous, reducing strong fluctuations seen in odd occupation numbers. The constant charge density for even N_{occ} suggests uniform electron pairing, characteristic of a non-magnetic, correlated metallic state. As seen, the corresponding spin densities in these cases are zero at each atomic site [Fig. 6(b)], consistent with

singlet-paired electrons forming a spin-balanced state. It is worth noting that we omit the adiabatic simulation results for charge and spin densities, as well as charge and spin correlations, at $N_{\text{occ}} = 4$ and 8 in Fig. 6, due to the vanishing energy gap $\Delta_{\text{min}}(\eta)|_{\eta \rightarrow 0} \rightarrow 0$, as defined in Eq. (5). This zero gap prevents the adiabatic evolution from reaching the true ground state within a practical time frame for these two configurations.

To complete our investigation, we now examine the charge correlations $C_{0,j}^c$ and spin correlations $C_{0,j}^s$ for different values of N_{occ} as depicted in Figs. 6(c) and 6(d), respectively. Due to particle-hole symmetry between states below and above half-filling, we present results only for $N_{\text{occ}} = 2, 3, \dots, 6$. As seen in Fig. 6(c), the charge correlations are negative across all sites and N_{occ} . This indicates anti-correlated charge fluctuations: if site $j = 0$ has a higher-than-average electron density, site j tends to have a lower-than-average density, driven by the repulsive interaction U_0 . For all N_{occ} , the charge correlations at sites $j = 1$ and $j = 5$ are the most negative, indicating strong anti-correlation with site $j = 0$. In a hexagonal geometry [Fig. 1(a)], sites $j = 1$ and $j = 5$ are nearest neighbors to site $j = 0$, suggesting that charge anti-correlations are strongest at these distances. For sites $j = 2, 3, 4$, weaker anti-correlations are observed, as they are farther from site $j = 0$. A symmetric trend in charge correlations is evident for all N_{occ} , consistent with the underlying hexagonal structure. However, this symmetry is exact for even N_{occ} and slightly broken for odd N_{occ} , likely due to an influence from the fermionic parity or interaction effects in the system. For $N_{\text{occ}} = 6$ (purple), the system is at half-filling, where electron repulsion is maximized. This leads to strongest anti-correlations, as electrons experience enhanced localization due to Coulomb interactions. This behavior is characteristic of a Mott-like insulating state, where charge movement is suppressed, and each site tends to be occupied by one electron on average. For $N_{\text{occ}} = 2$ (blue), the system exhibits the weakest charge anti-correlations since it is far from half-filling. In this regime, electrons have more available empty sites, allowing them to easily avoid each other, reducing charge correlations.

Figure 6(d) presents the corresponding spin correlations for the charge correlations shown in Fig. 6(a). The evolution of spin correlations with increasing electron occupation number N_{occ} reveals key signatures of electronic interactions and magnetic ordering in the moderately correlated Hubbard model with $U_0 = 3$ and $t = 1$. At low filling, spin correlations remain weakly negative ($N_{\text{occ}} = 2, 3$), suggesting a weak tendency toward antiferromagnetism (AFM) due to the lack of a well-defined spin structure. As N_{occ} increases, spin correlations transition from weak, uniformly negative values at low filling to a stronger alternating pattern at half-filling. This progression reflects the increasing influence of e-e interactions, leading to the emergence of short-range AFM. At $N_{\text{occ}} = 6$ (half-filling), the system exhibits its strongest

AFM correlations, characteristic of a Mott-like insulating state where Coulomb repulsion dominates charge fluctuations.

Finally, we conclude this section by briefly discussing the IQPE algorithm and adiabatic quantum simulation in simulating the Hubbard model on a six-site graphene hexagon. As demonstrated, the strong quantitative agreement between exact diagonalization and noiseless IQPE simulations highlights the accuracy and reliability of the IQPE method in capturing GSE and, more generally, the eigenvalues of strongly correlated systems. In the presence of interactions, IQPE remains highly accurate, even when using SDs as initial states. On the other hand, adiabatic state preparation proves to be an efficient approach for computing local observables, such as charge and spin densities, as well as charge and spin correlations. However, the time evolution operator in Eq. (5) plays a crucial role in the success of quantum simulations. Notably, for $N_{\text{occ}} = 4$ and 8, the algorithm fails to converge to the exact GSE due to the behavior of the minimum energy gap $\Delta_{\text{min}}(\eta)|_{\eta \rightarrow 0}$, which leads to an infinitely long evolution time—a fundamental limitation of adiabatic methods in such cases.

B. Noisy simulation and experiment

Studying the Hubbard model on real quantum hardware is essential for evaluating the practical feasibility of quantum algorithms like IQPE and adiabatic quantum simulation under realistic conditions, where gate errors, decoherence, and qubit connectivity constraints can significantly degrade performance compared to noiseless simulations that confirm their accuracy. To systematically analyze these effects, we construct a noise model tailored to `ibm_strasbourg`'s properties, incorporating three dominant noise channels—depolarizing errors, thermal relaxation errors, and readout errors—reflecting the primary error mechanisms in superconducting qubit systems, and use it to investigate how noise, error rates, and circuit depth limitations impact the accuracy and reliability of IQPE in estimating GSEs of quantum systems.

Depolarizing errors (gate infidelity) model the infidelity of quantum gate operations, capturing the random perturbations that occur during gate execution. In our noise model, single-qubit gates (e.g., X) and two-qubit gates (e.g., ECR) are assigned depolarizing channels with error probabilities derived from `ibm_strasbourg`'s median gate errors: $p_1 = 2.230 \times 10^{-4}$ for single-qubit gate and $p_2 = 7.986 \times 10^{-3}$ for two-qubit gates. This noise type simulates a process where, with a given probability, the qubit's state is replaced by a completely mixed state, effectively applying Pauli X , Y , or Z errors with equal likelihood. Depolarizing errors are particularly significant for two-qubit gates, which exhibit higher error rates due to their longer duration and complexity. In the context of IQPE, these errors may degrade the precision of controlled operations, potentially leading to phase es-

timization inaccuracies.

Thermal relaxation errors account for the decoherence that qubits experience due to interactions with their environment, both during active gate operations and idle periods. Parameterized by the hardware's T_1 (energy relaxation time, $\sim 300 \mu\text{s}$) and T_2 (dephasing time, $\sim 160 \mu\text{s}$), this noise channel models two processes: relaxation, where an excited qubit ($|1\rangle$) decays to the ground state ($|0\rangle$), and dephasing, where phase coherence in superpositions is lost. We incorporate gate durations, t_1 ($\sim 60 \text{ ns}$) for single-qubit gates and t_2 ($\sim 660 \text{ ns}$) for two-qubit gates, into the thermal relaxation model to simulate idle noise on inactive qubits, reflecting realistic circuit scheduling. For IQPE, which relies on precise phase accumulation over multiple iterations, thermal relaxation could introduce cumulative errors, especially in deeper circuits where idle times amplify decoherence effects.

Readout errors represent the misclassification of qubit states during measurement, a critical step in extracting results from quantum algorithms like IQPE. Using `ibm_strasbourg`'s median readout error of 1.953×10^{-2} , we model this noise as an asymmetric error channel with probabilities $P_{0|1} = 0.016$ and $P_{1|0} = 0.022$. This error type reflects the hardware's difficulty in distinguishing $|0\rangle$ from $|1\rangle$, often due to noise in the measurement apparatus or qubit relaxation during the measurement process (typically $1 \mu\text{s}$).

In the noiseless case, we modeled the full hexagonal ring with all six atomic sites to precisely capture the complete lattice connectivity and electronic interactions of the graphene structure. For the noisy simulations emulating IBM QPUs, however, we reduce the system register to $N = 3$ atomic sites. This reduction in qubit count ensures simulations remain fast and feasible, enabling a detailed investigation of noise effects—depolarizing errors, thermal relaxation, and readout imperfections—on IQPE performance. The simulations remain calibrated to hardware-realistic parameters while still capturing the essential features of the graphene Hubbard model.

First, we analyze the impact of each noise type individually—excluding the influence of other errors—on the energy estimation accuracy of the IQPE algorithm. To do so, we isolate each noise parameter, vary it over a broad range, and plot the mean GSE (averaged over 50 runs with 50,000 shots each) along with its variance to assess improvements in accuracy and reliability. For this analysis, we focus on the GSE of a half-filled three-atomic-site structure at $U_0 = 3$.

Figure 7(a) depicts the GSE as a function of single-qubit (p_{1q} , blue) and two-qubit (p_{2q} , red) depolarizing error rates. The result is expressed as the factor of `ibm_strasbourg`'s median gate errors p_1 and p_2 . The exact GSE is -1.545 , indicated by the orange dashed line. For small error rates ($p_{1q} = p_1/10, p_1/5$), the estimated GSE remains close to the exact value, with minimal variance, indicating that the algorithm is robust to small single-qubit gate errors. As p_{1q} increases, the

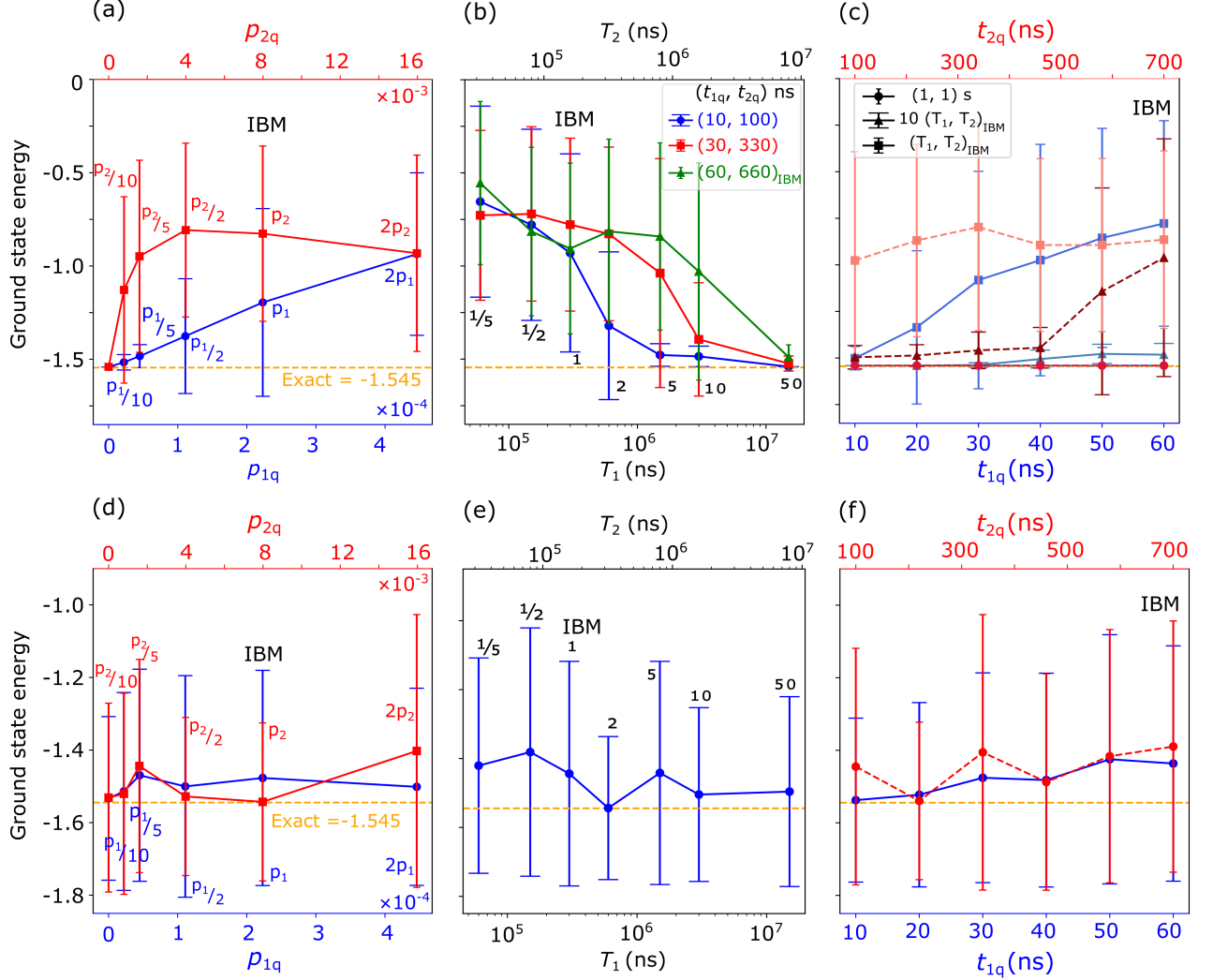


FIG. 7. The upper panels show the effect of each noise parameter on IQPE estimation of the GSE for a half-filled three-atomic-site Hubbard model, assuming all other noise channels are absent or set to their ideal values. (a) Effect of depolarizing errors – Mean GSE (solid lines) and its variance (shaded regions, representing standard deviation across 50 runs with 50,000 shots each) are plotted as functions of single-qubit (p_{1q} , lower axis) and two-qubit (p_{2q} , upper axis) depolarizing errors, expressed as factors of `ibm_strasbourg`'s median gate errors (p_1 and p_2). The exact GSE (-1.545) is shown by the orange dashed line. (b) Effect of thermal relaxation times – Mean GSE and variance as a function of T_1 (lower axis) and T_2 (upper axis) for different gate duration pairs (t_{1q}, t_{2q}): (10, 100) ns (blue circles), (30, 330) ns (red squares), and (460, 660) ns (green triangles). The results are presented for a range of (T_1, T_2) values, each scaled from the `ibm_strasbourg` baseline by factors of $[1/5, 1/2, 1, 2, 5, 10, 50]$. (c) Effect of gate durations – Mean GSE and variance as a function of single-qubit gate duration (t_{1q} , lower axis, blue) and two-qubit gate duration (t_{2q} , upper axis, red) for three sets of thermal relaxation parameters: $(T_1, T_2) = (1, 1)$ s (ideal, circles), $10 \times (T_1, T_2)_{\text{IBM}}$ (triangles), and $(T_1, T_2)_{\text{IBM}}$ (squares). Bluish solid lines represent t_{1q} variations, while reddish dashed lines represent t_{2q} variations. The lower panels illustrate the impact of (d) depolarizing errors, (e) thermal relaxation times, and (f) gate durations on IQPE GSE estimation, each evaluated while keeping the other noise parameters fixed at `ibm_strasbourg`'s baseline values.

estimated GSE deviates from the exact value, showing a smooth, monotonic increase with larger variance. In contrast, two-qubit errors have a markedly more disruptive impact—even at low error rates—shifting the estimated GSE to higher values and causing a sharp increase in variance. This behavior highlights the critical importance of two-qubit gate fidelity for achieving accurate GSE esti-

mates in NISQ-era simulations of quantum many-body systems like the Hubbard model, where multi-qubit interactions are essential for capturing complex electron correlations.

Figure 7(b) illustrates the mean estimated GSE as a function of thermal relaxation times (T_1, T_2) for different single- and two-qubit gate durations (t_{1q}, t_{2q}), as indi-

cated in the figure. The GSE is presented for a range of (T_1, T_2) values, each scaled from the baseline values of the `ibm_strasbourg` quantum processor by factors of $[1/5, 1/2, 1, 2, 5, 10, 50]$. For short coherence times, below the IBM baseline values, all gate durations result in substantially overestimated GSEs, reflecting significant decoherence effects. Beyond the baseline values, the GSE for the shortest gate durations (blue) drops sharply and converges towards the exact GSE (orange dashed line) as the T_1 and T_2 increase, reflecting reduced error rates. In contrast, the intermediate (red) and current IBM (green) gate durations yield progressively higher GSE estimates up to approximately 5 times the IBM baseline for T_1 and T_2 , indicating increased sensitivity to thermal noise at these scales. However, beyond this point, the GSE estimates for these longer gate durations gradually decrease, eventually converging to the exact GSE at around 50 times the baseline (T_1, T_2) values. This suggests a threshold behavior, where the coherence times become sufficiently long to suppress the dominant relaxation errors, resulting in accurate GSE estimation regardless of gate duration. Note that the shortest gate durations result in high variance up to approximately 2 times the IBM baseline (T_1, T_2) values. Beyond this point, the variance decreases significantly as coherence times improve, indicating more consistent and accurate GSE estimation. For the intermediate and IBM gate durations, a substantial reduction in variance is also observed beyond 10 times the (T_1, T_2) baseline values.

Shown in Fig. 7(c) illustrates the estimated GSE as a function of single-qubit (t_{1q} , lower axis, blue) and two-qubit (t_{2q} , upper axis, red) gate durations for three different thermal relaxation parameter sets (T_1, T_2) : (1, 1) s (circles), representing effectively error-free coherence times, $10 \times (T_1, T_2)_{\text{IBM}}$ (triangles), representing ten-fold enhanced IBM coherence times, and $(T_1, T_2)_{\text{IBM}}$ (squares), representing typical IBM coherence times. Bluish solid lines represent t_{1q} variations, while reddish dashed lines represent t_{2q} variations. For the ideal case, the GSE estimates remain relatively stable and close to the exact value, across the full range of gate durations, reflecting minimal decoherence effects. At $10 \times (T_1, T_2)_{\text{IBM}}$, the GSE remains relatively stable over the full range of t_{1q} values (bluish triangles), showing only minor deviations from the exact GSE, reflecting the robustness of single-qubit operations at extended coherence times. However, as a function of t_{2q} (reddish triangles), the GSE exhibits significant overestimation and high variance beyond approximately $t_{2q} = 450$ ns, highlighting the cumulative impact of longer two-qubit gate durations on phase fidelity. For the IBM baseline coherence times $(T_1, T_2)_{\text{IBM}}$ (blue, squares), the GSE increases gradually from near the exact value at the shortest $t_{1q} = 10$ ns to approximately -0.8 at $t_{1q} = 60$ ns, reflecting the increasing phase error with longer gate durations. As a function of t_{2q} (reddish squares), the GSE exhibits a more pronounced degradation, dropping to approximately -1.0 at the shortest t_{2q} values and showing a

gradual recovery with increasing t_{2q} . This trend indicates the greater vulnerability of multi-qubit gates to thermal relaxation effects, where the cumulative impact of error channels can significantly degrade the overall phase coherence, leading to overestimated GSE values. Our investigation (not shown here) shows that the IQPE algorithm is robust to a wide range of readout errors $[0, 0.2]$.

In the lower panel of Fig. 7, we investigate the impact of each noise on IQPE GSE estimation, while keeping the other parameters fixed at `ibm_strasbourg`'s baseline values, reflecting a more realistic device noise environment. In Fig. 7(d), the GSE estimates remain closer to the exact value across a wider range of p_{1q} and p_{2q} values compared to the isolated depolarizing error cases [Fig. 7(a)], indicating a partial compensation from other noise sources. However, the GSE still drifts upward at higher error rates, reflecting the cumulative effect of multi-channel noise. The error bars reflect high variance for all range of p_{1q} and p_{2q} values, indicating significant uncertainty in GSE estimates. Compared to the isolated noise plots, the GSE here shows less severe overestimation for similar p_{1q} and p_{2q} ranges, emphasizing the complex interplay between multiple noise sources in practical NISQ devices.

Figure 7(e) presents the mean estimated GSE as a function of thermal relaxation times (T_1, T_2) , with other noise parameters fixed at typical IBM values. The data are plotted for various T_1, T_2 , scaling factors relative to the IBM baseline as shown in the plot. Unlike the isolated thermal relaxation case [Fig. 7(b)], the GSE in Fig. 7(e), remains relatively stable across the entire range of T_1 and T_2 values, with a mean close to the exact value. Despite the stable mean, the error bars remain consistently large across the range, reflecting significant uncertainty in GSE estimates.

In Fig. 7(f), the estimated GSE exhibits an oscillatory, linear-like overestimation as a function of both t_{1q} and t_{2q} , with the effect being more pronounced for the two-qubit gate durations. The larger amplitude of oscillations observed along the t_{2q} axis further underscores the heightened sensitivity of two-qubit gates to duration-induced decoherence, consistent with their more complex entangling nature and higher error rates.

The collective analysis of the noise plots reveals a critical insight into the interplay between various quantum noise sources and their impact on the GSE estimation using the IQPE algorithm. While single-qubit depolarizing errors (p_{1q}) generally induce smaller, more controlled deviations in the GSE, two-qubit errors (p_{2q}) exhibit a substantially larger and less predictable impact, reflecting the higher sensitivity of entangling gates to noise. The thermal relaxation times (T_1, T_2) also play an axial role, where longer coherence times significantly suppress energy overestimations, but only if the gate durations remain sufficiently short. This points to the importance of optimizing both coherence and gate fidelity in reducing energy errors. Taken together, these findings highlight the need for careful noise mitigation strategies in near-term quantum devices, particularly emphasizing

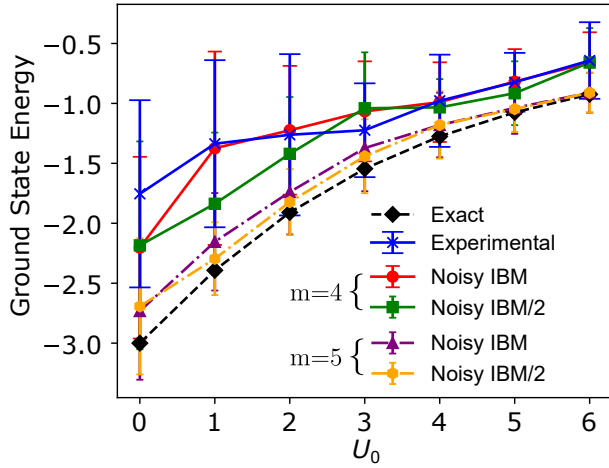


FIG. 8. GSE as a function of on-site interaction strength U_0 for a half-filled three-atomic-site Hubbard model. The plot compares results from exact diagonalization (black diamonds, dashed line), experimental runs on `ibm.strasbourg` quantum hardware (blue “x”), noisy simulations using IBM-calibrated noise parameters (red circles), and simulations with noise parameters reduced by a factor of 2 (green squares). All results use $m = 4$ and $N_{\text{trot}} = 12$, with error bars representing the standard deviation across 20 runs of 10,000 shots each. The purple and orange dotted-dashed lines show noisy simulation results with improved run parameters: $m = 5$, $N_{\text{trot}} = 15$, averaged over 50 runs with 50,000 shots each.

the reduction of two-qubit error rates and the extension of coherence times to achieve reliable GSE estimates for complex quantum systems like the Hubbard model.

Finally, we execute the IQPE algorithm on IBM’s real quantum hardware, `ibm.strasbourg`, and obtained the GSE for a half-filled three-atomic-site structure as a function of the on-site interaction U_0 , as shown in Fig. 8. Due to current hardware limitations, we use a binary precision of $m = 4$ and a Trotter step number of $N_{\text{trot}} = 12$. We also include results from noise simulations based on `ibm.strasbourg`’s hardware-calibrated noise parameters, along with simulations using noise parameters reduced by a factor of two, while keeping the same binary precision and Trotter step number. In all cases, the results are averaged over 20 runs with 10,000 shots each. The dashed line represents the exact diagonalization results. Experimental data from IBM quantum hardware (blue “x”) closely follow the noisy simulation results with IBM-calibrated noise parameters (red circles), particularly for higher U_0 values, although both consistently overestimate the GSE compared to the exact solution due to accumulated noise effects. Notably, the green triangles—representing simulations with improved (halved) noise levels—show a clearer approach to the exact curve, in the weakly interacting regime ($U_0 \lesssim 3$), suggesting that better hardware fidelity can improve quantum simulation accuracy. Across all cases, the error bars indicate remarkable variance at small U_0 , highlighting greater sensitivity to noise in the weakly correlated regime. As

seen, however, all cases closely follow each other with reduced variance at $U_0 \gtrsim 3$, indicating that the impact of noise diminishes in the strong interaction regime. The difference in noise sensitivity across U_0 can be attributed to the circuit complexity tied to the Hamiltonian structure. In the kinetic-dominated regime, non-commuting terms and Z_{JW} string lead to deeper, noisier circuits, whereas in the interaction-dominated regime, the commuting, diagonal nature of the interaction terms allows for more noise-resilient simulations. Implementing the noisy simulations with improved run parameters— $m = 5$ and $N_{\text{trot}} = 15$, averaged over 50 runs with 50,000 shots each—yields GSE values that closely match the exact result, as shown by the purple (IBM-calibrated noise) and orange (halved noise) dotted-dashed lines in Fig. 8. This comparison highlights the impact of hardware noise and parameter optimization on the accuracy of IQPE-based energy estimation.

IV. CONCLUSION AND REMARKS

In this work, we investigated the ground state properties of the Hubbard model on a six-site graphene hexagon using quantum simulation techniques. The study leveraged the IQPE algorithm and adiabatic quantum simulation, implemented via noiseless, noisy, and real quantum hardware simulations.

The noiseless simulations confirmed the capability of the IQPE algorithm to accurately reproduce the exact GSE, demonstrating its effectiveness for correlated fermionic systems such as the Hubbard model. Notably, our investigation revealed that initializing the IQPE with a single Slater determinant is sufficient to recover the correct ground state eigenvalue in small-scale Hubbard systems. Furthermore, to probe local observables such as charge and spin correlations, we employed adiabatic quantum simulation, which yielded results in excellent agreement with those obtained from exact diagonalization.

We considered noisy simulations in two scenarios. First, we evaluated the impact of each noise type in isolation, excluding all other errors, to assess their individual effects on IQPE energy estimation. Second, we studied each noise type while keeping the others fixed at IBM’s baseline values, reflecting a more realistic hardware noise environment. To reduce computational cost, the system size was limited to $N = 3$ atomic sites.

In the idealized context, we found thermal relaxation and two-qubit gate errors to be the most detrimental, causing significant energy overestimations and high variances. Longer gate durations also degraded performance, particularly for two-qubit operations, highlighting their critical role in IQPE accuracy. In contrast, readout errors were found to have a negligible impact on the overall accuracy within the scope of our simulations. Compared to the full-noise simulations, these idealized studies revealed more systematic and interpretable trends, offer-

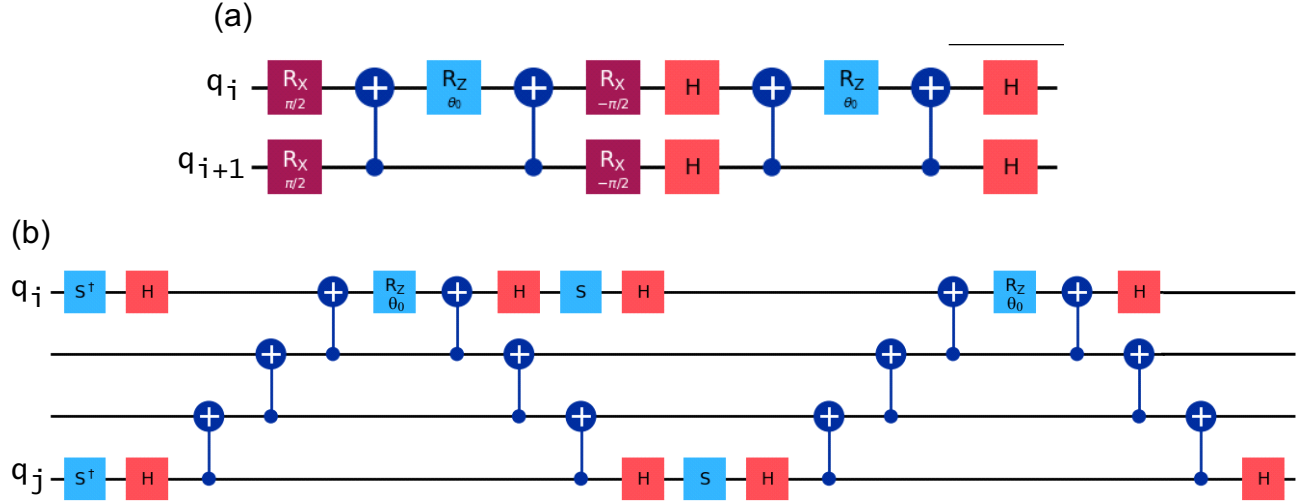


FIG. 9. Quantum circuit to implement time evolution under the hopping term $h_0 = -\gamma_0(a_{i\sigma}^\dagger a_{j\sigma} + a_{j\sigma}^\dagger a_{i\sigma})$. The time step is $\theta_0 = -\gamma_0 t$. Panel (a) shows the quantum circuit corresponding to the hopping term for two adjacent atomic sites labeled sequentially as i and $i + 1$. Panel (b) depicts the circuit for two adjacent sites, with non-sequential labeling.

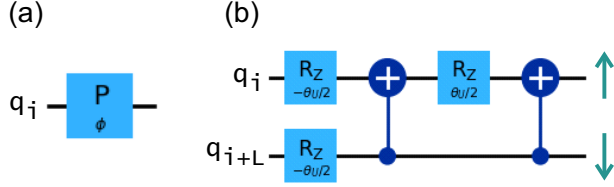


FIG. 10. Quantum circuits to implement time evolution for (a) the number operator $n_{i\sigma} = a_{i\sigma}^\dagger a_{i\sigma}$ and (b) on-site interaction term $U_0 n_{i\sigma} n_{j\sigma'}$. The time step is $\theta_U = U_0 t$.

ing clearer diagnostics for performance bottlenecks. They highlight that even in the absence of compounding errors, individual noise sources—particularly two-qubit gate imperfections and short coherence times—pose fundamental challenges to accurate quantum simulation in the NISQ regime.

In the second scenario, the GSE shows less severe overestimation across a wider range of studied noise parameter values compared to the isolated cases, indicating a partial compensation from other noise sources. In this case, our analysis showed that two-qubit gate errors and durations were the most harmful and unpredictable, significantly shifting GSE estimates and increasing variance. Regarding thermal relaxation effects, increasing T_1 and T_2 coherence times generally improved GSE accuracy. However, the benefits were more pronounced when gate durations were short, highlighting the interplay between coherent control and decoherence timescales.

Finally, direct execution on quantum hardware revealed that the IQPE algorithm can reliably estimate GSEs on real quantum hardware, though its accuracy is influenced by hardware noise and circuit complexity. While both experimental and noisy simulations tend to overestimate the GSE—especially in the weakly inter-

acting regime due to deeper circuits and greater noise sensitivity—simulations with reduced noise and improved parameters show clear convergence toward exact values. Notably, the impact of noise diminishes in the strongly interacting regime, where the Hamiltonian structure leads to shallower, more robust circuits. These findings emphasize the importance of hardware fidelity and parameter tuning for enhancing quantum simulation accuracy.

ACKNOWLEDGMENTS

This work is supported by the National Research Foundation of Korea (grant numbers NRF-2022M3K2A108385811, RS-2023-00257561).

APPENDIX: CIRCUITS FOR THE HUBBARD HAMILTONIAN

The unitary evolution under the hopping term h_0 , represented in Eq. (7) in the main text, is expressed as

$$\mathcal{U}_0(t) = \exp(-ih_0 t) = \exp\left[-i\frac{\theta_0}{2}(X_i X_j + Y_i Y_j)Z_{jW}\right], \quad (\text{A1})$$

whose quantum circuit is illustrated in Fig. 9. Figure 9(a) shows the circuit for two adjacent atomic sites, labeled sequentially as i and $i + 1$, while Fig. 9(b) depicts the circuit for two adjacent atomic sites with non-sequential labeling. The time step is $\theta_0 = -\gamma_0 t$.

The quantum circuit for the unitary evolution under the number operator (Eq. (8) in the main text)

$$\mathcal{U}_n(t) = \exp(-ia_i^\dagger a_i t) = \exp\left[-i\frac{1}{2}(I_i - Z_i)t\right], \quad (\text{A2})$$

is shown in Fig. 10(a), which can be considered as a Phase gate defined as $P(\phi) = \begin{bmatrix} 1 & 0 \\ 0 & e^{i\phi} \end{bmatrix}$ with the phase shift of $\phi = -t$.

The on-site interaction term is expressed in Eq. (9),

and its unitary evolution is given by

$$\begin{aligned} \mathcal{U}_U(t) &= \exp(-iU_0 n_i n_j t) \\ &= \exp \left[-i \frac{\theta_U}{4} (I_i I_j - I_i Z_j - Z_i I_j + Z_i Z_j) \right], \quad (\text{A3}) \end{aligned}$$

with the corresponding quantum circuit depicted in Fig. 10(b). Here, the time step is $\theta_U = U_0 t$. Note that due to the commutativity of interaction terms in the Hubbard model, they can be applied simultaneously.

-
- [1] I. M. Georgescu, S. Ashhab, and F. Nori, Quantum simulation, *Rev. Mod. Phys.* **86**, 153 (2014).
 - [2] B. Bauer, D. Wecker, A.J. Millis, M. B. Hastings, and M. Troyer, Hybrid quantum-classical approach to correlated materials, *Phys. Rev. X* **6**, 031045 (2016).
 - [3] B. Bauer, S. Bravyi, M. Motta, and G. K.-L. Chan, Quantum algorithms for quantum chemistry and quantum materials science, *Chem. Rev.* **120**, 12685 (2020).
 - [4] J. Hubbard, Electron correlations in narrow energy bands, *Proc. R. Soc. A* **276**, 238 (1963).
 - [5] F. H. L. Essler, H. Frahm, F. Göhmann, A. Klümper, and V. E. Korepin, *The one-dimensional Hubbard model*, (Cambridge University Press, 2005).
 - [6] D. J. Scalapino, “Numerical studies of the 2D Hubbard model” In *Handbook of High-Temperature Superconductivity: Theory and Experiment*, (Springer, New York, 2007), pp. 495–526.
 - [7] D. J. Scalapino, A common thread: The pairing interaction for unconventional superconductors, *Rev. Mod. Phys.* **84**, 1383 (2012).
 - [8] J. P. F. LeBlanc, A. E. Antipov, F. Becca *et al.*, Solutions of the two-dimensional Hubbard model: benchmarks and results from a wide range of numerical algorithms, *Phys. Rev. X* **5**, 041041 (2015).
 - [9] M. Qin, T. Schäfer, S. Andergassen, P. Corboz, and E. Gull, The Hubbard model: A computational perspective, *Annu. Rev. Condens. Matter Phys.* **13**, 275 (2022).
 - [10] N. F. Mott, The basis of the electron theory of metals, with special reference to the transition metals, *Proc. Phys. Soc. A* **62**, 416 (1949).
 - [11] P. A. Lee, From high temperature superconductivity to quantum spin liquid: progress in strong correlation physics, *Rep. Prog. Phys.* **71**, 012501 (2008).
 - [12] S. Yamada, T. Imamura and M. Machida, 16.447 TFlops and 159-Billion-dimensional exact-diagonalization for trapped Fermion-Hubbard model on the earth simulator, SC ’05: Proceedings of the 2005 ACM/IEEE Conference on Supercomputing, IEEE, (2005).
 - [13] U. Schollwöck The density-matrix renormalization group *Rev. Mod. Phys.* **77**, 259 (2005).
 - [14] E.M. Stoudenmire, Steven R. White, Studying two dimensional systems with the density matrix renormalization group, *arXiv:1105.1374*, (2011).
 - [15] R. Somma, G. Ortiz, J. E. Gubernatis, E. Knill, and R. Laflamme, Simulating physical phenomena by quantum networks, *Phys. Rev. A* **65**, 042323 (2002).
 - [16] D. Wecker, M. B. Hastings, N. Wiebe, B. K. Clark, C. Nayak, and M. Troyer, Solving strongly correlated electron models on a quantum computer, *Phys. Rev. A* **92**, 062318 (2015).
 - [17] D. Wecker, M. B. Hastings, and M. Troyer, Progress towards practical quantum variational algorithms, *Phys. Rev. A* **92**, 042303 (2015).
 - [18] Z. Jiang, K. J. Sung, K. Kechedzhi, V. N. Smelyanskiy, and S. Boixo, Quantum algorithms to simulate many-body physics of correlated fermions, *Phys. Rev. Appl.* **9**, 044036 (2018).
 - [19] J.-M. Reiner, F. Wilhelm-Mauch, G. Schön, and M. Marthaler, Finding the ground state of the Hubbard model by variational methods on a quantum computer with gate errors, *Quantum Sci. Technol.* **4**, 035005 (2019).
 - [20] C. Cade, L. Mineh, A. Montanaro, and S. Stanisic, Strategies for solving the Fermi-Hubbard model on near-term quantum computers, *Phys. Rev. B* **102**, 235122 (2020).
 - [21] Z. Cai, Resource estimation for quantum variational simulations of the Hubbard model, *Phys. Rev. Appl.* **14**, 014059 (2020).
 - [22] An application benchmark for fermionic quantum simulations, *arXiv:2003.01862*, (2020).
 - [23] B. A. Martin, P. Simon, and M. J. Rančić, Simulating strongly interacting Hubbard chains with the variational Hamiltonian ansatz on a quantum computer, *Phys. Rev. Research* **4**, 023190 (2022).
 - [24] B. T. Gard and A. M. Meier, A classically efficient quantum scalable Fermi-Hubbard benchmark, *Phys. Rev. A* **105**, 042602 (2022).
 - [25] S. Stanisic, J.L. Bosse, F.M. Gambetta *et al.*, Observing ground-state properties of the Fermi-Hubbard model using a scalable algorithm on a quantum computer, *Nat. Commun.* **13**, 5743 (2022).
 - [26] T. Ayril, P. Besserve, D. Lacroix, and E. A. R. Guzman, Quantum computing with and for many-body physics, *Eur. Phys. J. A* **59**, 227 (2023).
 - [27] M. Cerezo, A. Arrasmith, R. Babbush *et al.*, Variational quantum algorithms, *Nat. Rev. Phys.* **3**, 625 (2021).
 - [28] E. Farhi, J. Goldstone, and S. Gutmann, A quantum approximate optimization algorithm, *arXiv:1411.4028* (2014).
 - [29] J. Tilly, H. Chen, S. Cao *et al.*, The Variational Quantum Eigensolver: A review of methods and best practices, *Phys. Rep.* **986**, 1 (2022).
 - [30] K. Blekos, D. Brand, A. Ceschini *et al.*, A review on Quantum Approximate Optimization Algorithm and its variants, *Phys. Rep.* **1068**, 1 (2024).

- [31] M. A. Nielsen and I. L. Chuang, *Quantum Computation and Quantum Information*, (Cambridge University Press, Cambridge, UK, 2010).
- [32] A. Yu. Kitaev, Quantum measurements and the Abelian Stabilizer Problem, arXiv:quant-ph/9511026 (1995).
- [33] D. S. Abrams and S. Lloyd, Simulation of many-body fermi systems on a universal quantum computer, Phys. Rev. Lett. **79**, 2586 (1997).
- [34] D. S. Abrams and S. Lloyd, Quantum algorithm providing exponential speed increase for finding eigenvalues and eigenvectors, Phys. Rev. Lett. **83**, 5162 (1999).
- [35] A. Aspuru-Guzik, A. D. Dutoi, P. J. Love, and M. Head-Gordon, Simulated quantum computation of molecular energies, Science **309**, 1704 (2005).
- [36] J. D. Whitfield, J. Biamonte, and A. Aspuru-Guzik, Simulation of electronic structure Hamiltonians using quantum computers, Mol. Phys. **109**, 735 (2011).
- [37] S. Parker and M. B. Plenio, Efficient factorization with a single pure qubit and $\log N$ mixed qubits, Phys. Rev. Lett. **85**, 3049 (2000).
- [38] M. Dobšíček, G. Johansson, V. Shumeiko, and G. Wendin, Arbitrary accuracy iterative quantum phase estimation algorithm using a single ancillary qubit: A two-qubit benchmark, Phys. Rev. A **76**, 030306(R) (2007).
- [39] L. Xiu-Mei, L. Jun, and S. Xian-Ping, Experimental realization of arbitrary accuracy iterative phase estimation algorithms on ensemble quantum computers, Chinese Phys. Lett. **24**, 3316 (2007).
- [40] Qiskit, <https://quantum.cloud.ibm.com/docs/en/guides>
- [41] A. Javadi-Abhari, M. Treinish, K. Krsulich, C. J. Wood, J. Lishman, J. Gacon, S. Martiel, P. D. Nation, L. S. Bishop, A. W. Cross, B. R. Johnson, and J. M. Gambetta, Quantum computing with Qiskit, arXiv:2405.08810 (2024).
- [42] IBM Quantum Platform, <https://quantum.cloud.ibm.com/>
- [43] A. K. Geim and K. S. Novoselov, The rise of graphene, Nat. Mater. **6**, 183 (2007).
- [44] A. H. Castro Neto, F. Guinea, N. M. R. Peres, K. S. Novoselov, and A. K. Geim, The electronic properties of graphene, Rev. Mod. Phys. **81**, 109 (2009).
- [45] J. Fernández-Rossier and J. J. Palacios, Magnetism in graphene nanoislands, Phys. Rev. Lett. **99**, 177204 (2007).
- [46] A. V. Rozhkov, G. Giavaras, Y. P. Bliokh, V. Freilikher, F. Nori, Electronic properties of mesoscopic graphene structures: Charge confinement and control of spin and charge transport, Phys. Rep. **503**, 77 (2011).
- [47] O. V. Yazyev, Emergence of magnetism in graphene materials and nanostructures, Rep. Prog. Phys. **73**, 056501 (2010).
- [48] A. D. Güçlü, P. Potasz, M. Korkusinski, and P. Hawrylak, Graphene quantum dots, (Springer, Berlin Heidelberg 2014).
- [49] D. G. de Oteyza and T. Frederiksen, Carbon-based nanostructures as a versatile platform for tunable π -magnetism, J. Phys.: Condens. Matter **34**, 443001 (2022).
- [50] G. Ortiz, J. E. Gubernatis, E. Knill, and R. Laflamme, Quantum algorithms for fermionic simulations, Phys. Rev. A **64**, 022319 (2001).
- [51] I. D. Kivlichan, J. McClean, N. Wiebe, C. Gidney, A. Aspuru-Guzik, G. K. -L. Chan, and R. Babbush, Quantum simulation of electronic structure with linear depth and connectivity, Phys. Rev. Lett. **120**, 110501 (2018).
- [52] E. Farhi, J. Goldstone, S. Gutmann, J. Lapan, A. Lundgren, and D. Preda, A quantum adiabatic evolution algorithm applied to random instances of an NP-complete problem, Science **292**, 472 (2001).
- [53] Qiskit Nature, <https://doi.org/10.5281/zenodo.7828767v>
- [54] N. Hatano and Masuo Suzuki, "Finding exponential product formulas of higher orders" In *Quantum annealing and other optimization methods*, (Springer, Berlin, Heidelberg, 2005) pp. 37-68.
- [55] P. Jordan and E. Wigner, Über das Paulische Äquivalenzverbot, Z. Phys. A. **47**, 631 (1928).
- [56] P. Weinberg and M. Bukov, QuSpin: a Python package for dynamics and exact diagonalisation of quantum many body systems. Part II: bosons, fermions and higher spins, SciPost Phys. **7**, 020 (2019).